SUPERFLUIDITY

Coherent vortex dynamics in a strongly interacting superfluid on a silicon chip

Yauhen P. Sachkou[1]*, Christopher G. Baker[1]*, Glen I. Harris[1]*, Oliver R. Stockdale[2], Stefan Forstner[1], Matthew T. Reeves[2], Xin He[1], David L. McAuslan[1], Ashton S. Bradley[3], Matthew J. Davis[1,2], Warwick P. Bowen[1]†

Quantized vortices are fundamental to the two-dimensional dynamics of superfluids, from quantum turbulence to phase transitions. However, surface effects have prevented direct observations of coherent two-dimensional vortex dynamics in strongly interacting systems. Here, we overcome this challenge by confining a thin film of superfluid helium at microscale on the atomically smooth surface of a silicon chip. An on-chip optical microcavity allows laser initiation of clusters of quasi–two-dimensional vortices and nondestructive observation of their decay in a single shot. Coherent dynamics dominate, with thermal vortex diffusion suppressed by five orders of magnitude. This establishes an on-chip platform with which to study emergent phenomena in strongly interacting superfluids and to develop quantum technologies such as precision inertial sensors.

S trongly interacting many-body quantum systems exhibit rich behaviors of significance to areas ranging from superconductivity (1) to quantum computation (2, 3), astrophysics (4–6), and even string theory (7). The first example of such a behavior, superfluidity, was discovered >80 years ago in cryogenically cooled liquid helium-4. It was found to persist even in very thin two-dimensional films, for which the well-known Mermin–Wagner theorem precludes condensation into a superfluid phase in the thermodynamic limit [see, e.g., discussion in (8)]. This apparent contradiction was resolved by Berezinskii, Kosterlitz, and Thouless (BKT), who predicted that quantized vortices allow a topological phase transition into superfluidity (9, 10). It is now recognized that quantized vortices dominate much of the two-dimensional dynamics of out-of-equilibrium superfluids even outside the regime of BKT superfluidity, including quantum turbulence (11) and anomalous hydrodynamics (12).

Recently, laser control and imaging of vortices in ultracold gases (13, 14) and semiconductor exciton-polariton systems (15, 16) have provided rich capabilities to study superfluid dynamics including, for example, the formation of collective quasi–two-dimensional vortex dipoles with negative temperature and large-scale order (17, 18) as predicted by Lars Onsager 70 years ago (19). However, these experiments are generally limited to the regime of weak interactions, where the Gross–Pitaevskii equation provides a microscopic model of the dynamics of the superfluid. The regime of strong interactions can be reached by tuning the atomic scattering length in ultracold gases (20–23), although three-body losses can limit the system lifetime (20). Superfluid helium, by contrast, exists naturally in this state, which offers the possibility of studying many-vortex dynamics over a much greater range of length and time scales (24). The strongly interacting regime is relevant for astrophysical superfluid phenomena such as pulsar glitches (6) and superfluidity of the quark-gluon plasma in the early universe (5) and is highly challenging to treat theoretically (25, 26). The vortex dynamics in this regime are typically predicted using phenomenological vortex models. However, questions such as whether the vortices have inertia (27, 28), what is the precise nature of the forces they experience from the normal component of the fluid (29), and how to treat dissipation given the nonlocal nature of the vortex flow fields (8, 30) all remain to be conclusively answered. Moreover, point-vortex modeling offers limited insight into the processes of vortex creation and annihilation, which are crucial to understanding the dynamics of topological phase transitions.

Here, we report the observation of coherent dynamics of quasi–two-dimensional vortices in a strongly interacting superfluid. We achieve this by developing a microscale photonic platform to initialize vortex clusters in a few-nanometer-thick film of helium-4 on a silicon chip, confine them, and image their spatial distribution over time. Our experiments characterize vortex distributions through their interactions with resonant superfluid surface waves, taking advantage of ultraprecise sensing methods from cavity optomechanics (31–33). Microscale confinement greatly enhances the interactions and enables resolution of the dy-namics of few-vortex clusters in a single shot and tracked over many minutes as they interact, dissipate energy, and annihilate. We find that evaporative heating occurs, where the annihilation of low-energy vortices draws energy out of a background flow, causing a net increase in free-vortex kinetic energy as the system evolves.

Our experiments yield a vortex diffusivity five orders of magnitude lower than has been observed previously for unpinned vortices in superfluid helium films (34). This verifies that the diffusivity can become exceptionally small when operating at temperatures far below the superfluid transition temperature, as conjectured from extrapolation of 30-year-old experimental observations (8, 34). Therefore, the system operates well within the regime of coherent vortex dynamics, with the time scale for dissipation found to exceed the coherent evolution time by more than five orders of magnitude. The on-chip system reported here provides a platform with which to explore the dynamics of phase transitions and quantum turbulence in strongly interacting superfluids and to study how such fluids evolve toward thermal equilibrium and dissipate energy.

Nonequilibrium vortex clusters can be generated with laser light

Figure 1A shows a schematic of our experimental apparatus. A microscale optical ring cavity with laser-reflowed atomically smooth surface, conventionally known as a microtoroid (35), is placed inside a sealed sample chamber within a closed-cycle ^{3}He cryostat. The microtoroid confines light in whispering gallery mode resonances, which are excited through an optical nanofiber. The microtoroid is fabricated from silica, has a radius of $R = 30$ μm, and is suspended above a silicon chip by a pedestal that narrows to a radius of $r_p \sim 1$ μm where it contacts the bottom surface of the microtoroid (Fig. 1A, inset). The sample chamber is filled with ^{4}He gas at room temperature. The pressure is chosen so that the gas condenses directly into an unsaturated superfluid film at ~1 K. This film coats the inside of the chamber, including the optical microcavity (31, 36). Vortices and superfluid surface waves can coexist in the superfluid film and are geometrically confined to the surface of the microtoroid.

Our experiments operate with a superfluid film thickness of $d \sim 7.5$ nm and a temperature of $T \sim 500$ mK, well below the superfluid transition. In these conditions, the thickness far exceeds the superfluid healing length, such that the system is outside the regime of BKT superfluidity. However, from the hydrodynamic perspective, the system is quasi–two-dimensional because both the lowest-energy vertically propagating phonon modes and the lowest-energy Kelvin modes of vortices have

energies comparable to the thermal energy, so only a few of these modes are expected to be thermally excited [see section 1.1 of (37)].

We find experimentally that vortex clusters can be optically initialized on the surface of the microtoroid in several ways, including pulsing the intensity of the injected laser to induce superfluid flow through the "fountain effect" (36) and optomechanical driving of low-frequency surface waves by dynamical backaction (31). Both of these techniques induce flow that exceeds the superfluid critical velocity at the interface between the pedestal and the microtoroid. This triggers the generation of vortex pairs on the bottom surface of the microtoroid in close proximity to the pedestal (Fig. 1B). In the presence of a circular boundary, an ensemble of vortex pairs evolves into a metastable state characterized at high energies by a large-scale negative-temperature Onsager vortex dipole (17, 19) [see section 3.2 of (37)]. In our case, the microtoroid pedestal introduces a deep potential to which vortices can pin [see section 7 of (37)], qualitatively modifying the physics. Vortices of one sign become pinned, creating a macroscopic circulation, whereas vortices of the opposite sign evolve into a free-orbiting metastable cluster similar to the case without a pinning site [see section 3.2 of (37)].

The time scale within which a metastable state is reached can be estimated from the characteristic turnover time for internal rearrangement of the free-vortex cluster, $\tau \sim r_c^2/N\kappa$, where N is the number of free vortices, r_c is the radius of the cluster, and $\kappa = h/m_{He}$ is the circulation quantum, with m_{He} being the mass of a helium atom and h Planck's constant (38) [see section 3.2 of (37)]. Considering the case of two free vortices separated by the disk radius provides an upper bound to the turnover time of $\tau \lesssim 5$ ms. This is substantially faster than both the dissipation of the system and the temporal resolution of our measurements, which are ~1 min and 1 s, respectively. Consequently, the vortex cluster can be well approximated to exist in a metastable state throughout its evolution, with this state modified continuously by dissipation and in discrete steps by vortex annihilation events.

Each possible metastable state is uniquely characterized by the number of free vortices, kinetic energy, and angular momentum. Performing point-vortex simulations, we determine the possible metastable vortex distributions as a function of these three parameters [see section 3.2 of (37)]. In their metastable state, the free vortices exist in an orbiting horseshoe-shaped cluster separated from the origin, which, together with the macroscopic circulation, forms a vortex dipole. Figure 1C illustrates how the distribution of the cluster evolves as a consequence of changes in vortex number, kinetic energy, and angular momentum.

Interactions with third-sound allow vortex imaging

The interaction between light and vortices is extremely weak in superfluid helium because of its exceedingly low refractive index and the Angström scale of the vortex cores. This precludes direct optical imaging techniques. Furthermore, the tracer particles used to image vortex dynamics in bulk three-dimensional helium (24) are too large to be applied in thin films. Instead, in our experiments, the vortex dynamics are tracked through their influence on resonant superfluid third-sound waves that are also confined to the bottom surface of the microtoroid (Fig. 2A). Third-sound waves are surface waves analogous to shallow-water waves but with a restoring force provided by the van der Waals interaction with the substrate rather than gravity [see, e.g., (39)]. They also exist on the top surface of the microtoroid

but in this case are isolated from the vortices because of their physical separation [see section 2 of (37)]. We monitor the thermal excitations of third-sound modes in real time through their effect on the height of the superfluid film in the optical evanescent field of the microtoroid (31). This manifests as fluctuations of the phase of light confined inside the cavity, which are resolved through balanced homodyne detection implemented within a fiber interferometer (Fig. 1A). Frequency analysis of the output photocurrent reveals resonances with frequencies that are in good agreement with expectations for third-sound modes confined to a circular geometry [see sections 1 and 2 of (37)]. The resonances are Bessel modes, characterized by their radial m and azimuthal n mode numbers (41).

The vortex flow field causes Doppler shifts of the frequencies of the third-sound modes,
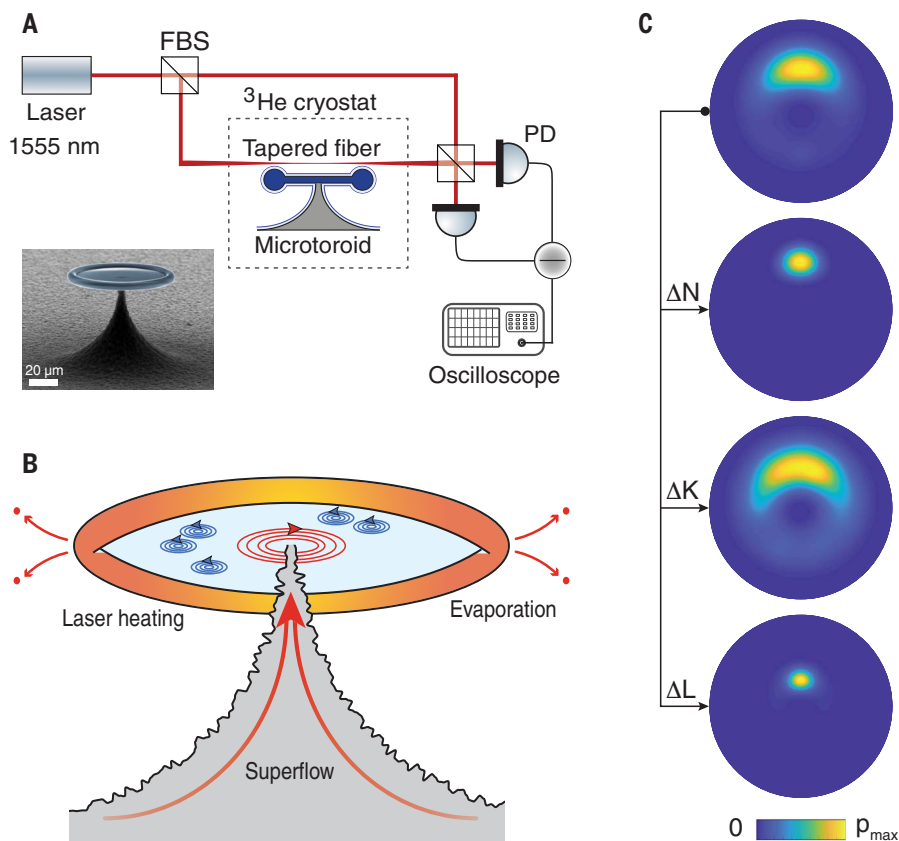
Fig. 1. Laser initialization of vortex clusters. (**A**) Experimental setup. A balanced homodyne detection scheme is implemented within a fiber interferometer. FBS, fiber beam splitter; PD, photodetector. Inset shows a scanning electron microscope image of the microtoroidal optical cavity used in the experiments. Scale bar, 20 μm. (**B**) Sketch of the vortex generation process. Laser heating of the microtoroid perimeter causes superfluid evaporation, followed by superflow (36). The flow exceeds the superfluid critical velocity at the top of the microtoroid pedestal, seeding the generation of vortex pairs. (**C**) Exemplar simulated metastable distributions showing the effects of vortex annihilation and of changes in total kinetic energy K and angular momentum L. The color map indicates the free-vortex probability density, with a maximum of $p_{max} = \{0.035, 0.075, 0.023, 0.12\}$ μm^{-2}, respectively, for the top to bottom metastable states. Top metastable state: $\{N,K,L\} = \{10, 0.43$ aJ, 120 ag μm^2 s$^{-1}\}$; second to top: $N \to 9$; second to bottom: $K \to 0.41$ aJ; and bottom: $L \to 44$ ag μm^2 s^{-1}.
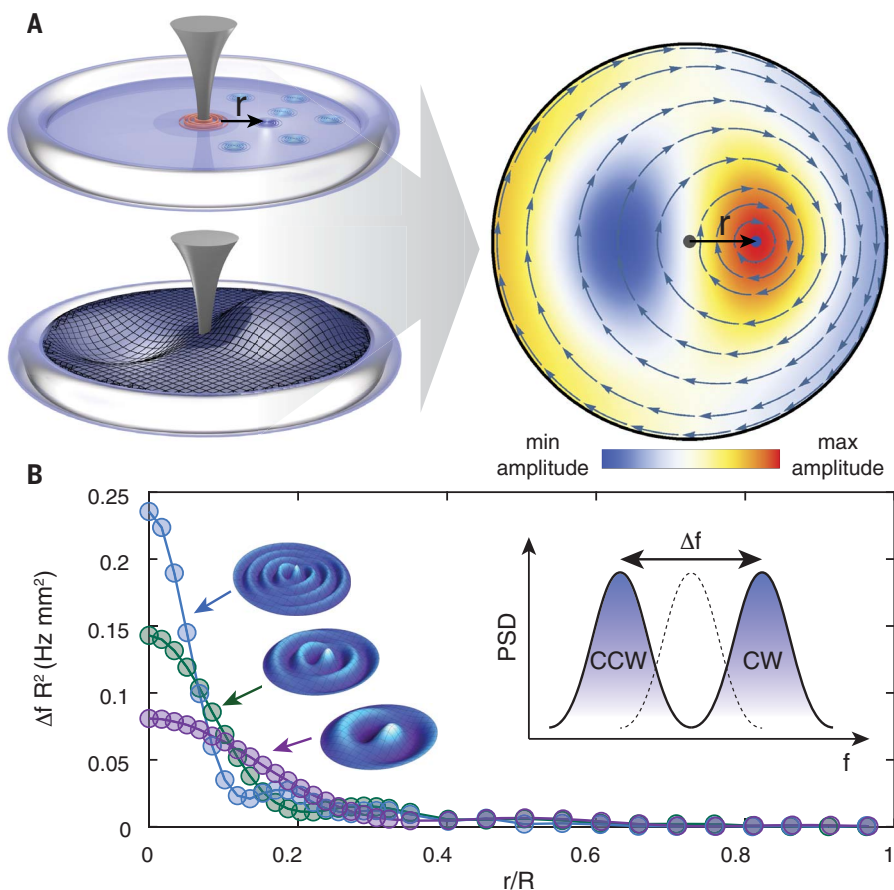
Fig. 2. Interactions between vortices and third-sound on a disk. (**A**) Top left: Free vortices (blue) and pinned circulation (red) on the bottom surface of the microtoroid. Bottom left: A third-sound mode on the same surface. The vortices and third-sound couple due to the superposition of their flow fields, shown on the right for the case of a single vortex (blue dot) offset from the disk origin by distance r. Here, the surface color represents the third-sound mode amplitude profile and the blue lines are vortex streamlines. Confinement within the same microscale domain enhances both the interaction rate between vortices and third-sound and the resulting frequency splitting between counterpropagating third-sound modes. (**B**) Normalized splitting per vortex for third-sound modes $(m,n) = (1,3)$, $(1,5)$, and $(1,8)$ calculated by finite-element modeling using the techniques detailed in (*40*) and outlined in section 2.1 of (*32*), with their respective spatial profiles. The inset schematically depicts the vortex-induced splitting Δf between clockwise and counterclockwise third-sound modes in the presence of a clockwise vortex, which would be observed as a function of frequency f in the power spectral density (PSD) of the optically measured superfluid motion.

lifting the degeneracy between clockwise and counterclockwise waves (Fig. 2). The magnitude of the frequency splitting induced by a vortex scales inversely with the area in which it is confined (*39, 40*). As such, the microscale confinement provided by our microtoroid allows greatly enhanced resolution compared with previous experiments (*39, 42*). The splitting also depends both on the position of the vortex and on the spatial profile of the third-sound mode, as shown for several modes in Fig. 2B. Despite the strong interactions between helium atoms, the phase coherence and incompressibility of the superfluid combine to ensure linearity. Therefore, the total flow field of a vortex cluster is given by the linear superposition of the flow of each constituent vortex. The total splitting between counter-rotating third-sound modes is then equal to the sum of the splittings generated by each vortex and by the macroscopic circulation pinned to the pedestal. We exploit this linearity, combined with the vortex position–dependent interaction and simultaneous measurements of splitting on several third-sound modes, to characterize the spatial distribution of vortex clusters in a manner analogous to experiments that use multiple cantilever eigenmodes to image the distribution of deposited nanoparticles (*43*).

Vortex clusters evolve coherently

To determine the instantaneous metastable vortex distribution from a single continuous measurement, we generate a nonequilibrium vortex cluster by optically initiating super-

critical flow. We then simultaneously measure the frequency splittings induced on the $(m,n) = (1,3)$, $(1,4)$, $(1,5)$, $(1,7)$, and $(1,8)$ third-sound modes as the cluster evolves over time, anticipating vortex-dipole decay as illustrated in Fig. 3A. As a representative example, Fig. 3B shows the observed power spectral density and frequency splitting of the $(1,7)$ third-sound mode at the start of the measurement run, just after the vortex cluster has been initialized [see section 2 of (*37*) for the initial power spectral densities of all modes]. Using the vortex position–dependent splitting function $\Delta f(r)$ (Fig. 2B), the frequency shifts expected on each of the third-sound modes are computed for all possible metastable distributions and compared with the observed shifts. This allows us to ascertain both the metastable state that most closely matches the observed frequency shifts at a given time, as well as the range of metastable states for which the shifts are statistically indistinguishable.

As shown for the initial metastable vortex distribution in Fig. 3C (colored circular points), we find excellent agreement between the observed frequency splittings and those obtained with the best-fit metastable distribution. Moreover, although the measurements only loosely constrain the angular momentum [see section 4.2 of (*37*)], we find that the statistical uncertainty in the number of free vortices and kinetic energy is relatively small. The free vortex number in the initial vortex dipole is statistically constrained to a value of either 16 or 17. For the case of 16 vortices, the total kinetic energy and angular momentum are constrained to $K = 0.8^{+0.2}_{-0.02}$ aJ and $L = 0.2^{+0.3}_{-0.07}$ fg μm^2 s^{-1}, respectively, whereas for 17 vortices, they are constrained to $K = 0.8^{+0.1}_{-0.03}$ aJ and $L = 0.3^{+0.05}_{-0.2}$ fg μm^2 s^{-1}. We are also able to determine the dipole separation, which in the case of 17 vortices is found to be $7.3^{+1.2}_{-0.8}$ μm.

Continuously monitoring the superfluid third-sound modes reveals that their splittings decay over a time scale on the order of minutes (Fig. 3C). The observed splittings are well characterized by a metastable vortex dipole throughout this entire decay process. By contrast, they are inconsistent with other vortex dynamics models such as expansion of a single-sign vortex cluster caused by either vortex-vortex interactions or diffusive hopping between pinning sites on the surface of the microtoroid [see section 4 of (*37*)].

The kinetic energy and free-vortex number of the metastable state are shown as a function of time for a single shot in Fig. 4, A and B (blue curves). The total kinetic energy of the dipole decays continuously with time as a consequence of weak dissipation. This decay occurs over a period of ~1 min, comparable to previous nonspatially resolved measurements of the decay of a persistent current (*44*). In our

experiments, the decay is accompanied by a reduction in the number of free vortices as vortex-vortex interactions and dissipation drive vortices into the center of the disk, where they can annihilate with quanta of circulation of opposite sign pinned to the pedestal. These dynamics are supported by point-vortex simulations (Fig. 4, C and D), which show good quantitative agreement with only the mutual friction coefficient α as a fitting parameter. The agreement between experiment and theory indicates that within experimental uncertainties, the vortex dynamics are consistent with a simple point vortex model including local phenomenological dissipation and without the need to introduce surface pinning sites, inertia to the vortex cores (27, 28), or an Iordanskii force between vortices and the normal component of the fluid (29).

The mutual friction coefficient quantifies the ratio of coherent to dissipative time scales in the superfluid dynamics and in our system is expected to be determined by a combination of temperature-dependent phonon- and ripplon-scattering processes, as well as surface roughness effects. From the fit, it is found to be $\alpha \sim 2 \times 10^{-6}$ [see section 3.3 of (37)]. A second experiment under similar conditions but with an initial free-vortex number of $N = 33^{+2}_{-1}$ is broadly consistent, yielding $\alpha \sim 3 \times 10^{-6}$ [see section 5 of (37)]. These values are similar to both measurements (45, 46) and theoretical predictions [see section 3.4 of (37)] for bulk superfluid helium, suggesting that surface effects are small despite the quasi–two-dimensional geometry. It has generally been thought that fast dissipative processes would preclude the observation of coherent dynamics in superfluid helium films. However, the mutual friction coefficient obtained here shows that this is not the case in general, with coherent dynamics dominating by more than five orders of magnitude. This is competitive with the best ultracold atom experiments, which typically achieve $\alpha \sim 6 \times 10^{-4}$ (17).

Nonequilibrium vortex dynamics is observed in a single shot

The pinning of vortices on the microtoroid pedestal results in a macroscopic circulation, as discussed above. The kinetic energy associated with the free vortex cluster is given by $K_{free} = K - K_{pinned}$, where $K_{pinned} = \rho d(N\kappa)^2 \ln(R/r_p)/4\pi$, the kinetic energy of the macroscopic circulation alone, with $\rho = 145$ kg/m^3 being the density of superfluid helium. K_{free} is shown for both our experimental data and simulations by the red curves in Fig. 4, A and C. During the first minute of evolution, it is negative and, notably, increases with time. The dynamics are characterized by steps up in energy during vortex annihilation events interspersed with a continuous dissipative decay.

The negativity of the free-vortex energy can be understood by considering the interference between the flow fields of a free vortex and the macroscopic circulation. Although the high flow velocity near the core of a free vortex introduces kinetic energy, the vortex flow field also cancels a component of the background flow. For a sufficiently large circulation, this cancellation effect dominates, leading to an overall negative energy cost to introducing the vortex cluster [see section 7.2 of (37)].

The increase in free-vortex energy over time can be explained by considering the process of vortex annihilation in a macroscopic background flow. To annihilate, a free vortex must reach the pedestal, where its contribution to the total kinetic energy is at a minimum. To do this, it gives up kinetic energy to the remaining free vortices. This process of removing low-energy vortices has been described as evaporative heating (18), in analogy to evaporative cooling of ultracold atomic ensembles. However, whereas standard evaporative heating can explain a per-vortex increase in kinetic energy, its effect is to reduce the net free-vortex kinetic energy (18). The physics is modified here by the presence of a macroscopic background flow. The annihilation of a free vortex with a pinned circulation quanta cancels a component of this flow, reducing its kinetic energy while leaving the total kinetic
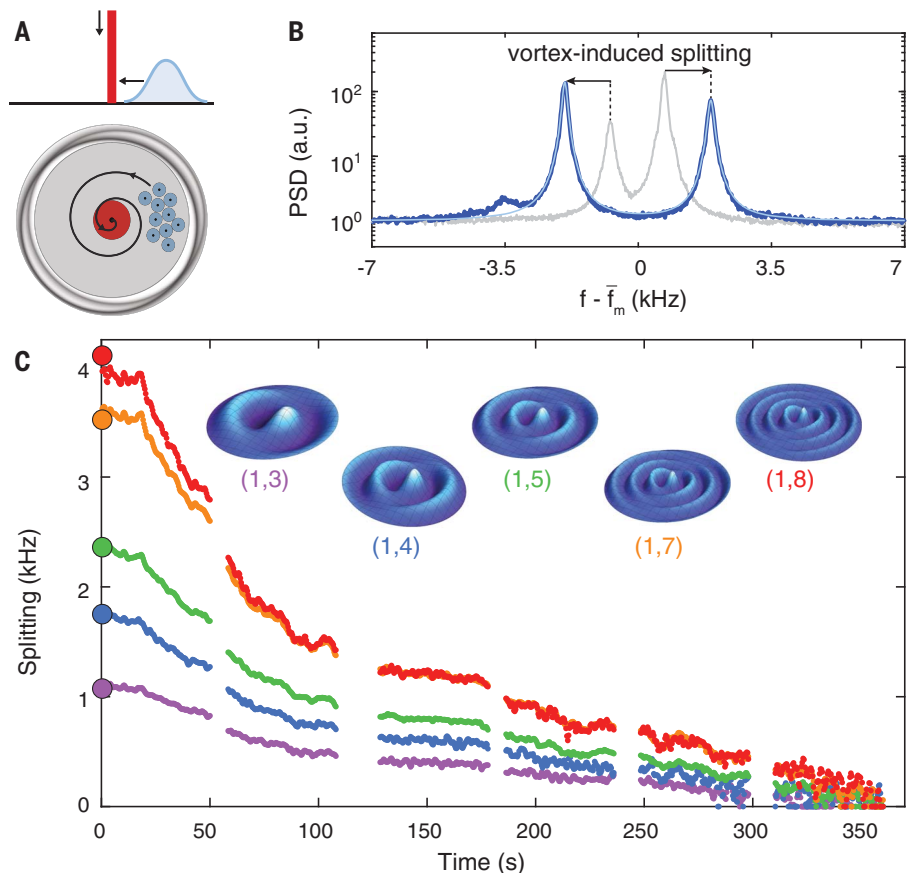
Fig. 3. Temporal dynamics of third-sound splitting. (**A**) Vortex-dipole decay process. Red indicates quantized circulation around the pedestal reduces due to annihilation events. Light blue indicates orbiting free-vortex cluster spirals toward the origin due to dissipation. Dissipation is exaggerated for clarity. (**B**) Experimental splitting observed in the PSD of the $(m,n) = (1,7)$ third-sound mode pair immediately after vortex-dipole initialization. Gray spectra are the third-sound mode pair without vortices. The residual splitting in these unperturbed spectra is caused by irregularities in the circularity of the microtoroid that break the degeneracy between standing-wave Bessel modes (31) and is accounted for in data processing [see section 1.3 of (37)]. f is the frequency of superfluid motion; $\bar{f}_m$ is the mean resonance frequency of third-sound mode pair. (**C**) Temporal decay of splitting of the $(m,n) = (1,8)$, (1,7), (1,5), (1,4), and (1,3) third-sound modes (top to bottom traces, respectively). These specific modes were chosen because of the high signal-to-noise ratio of their PSDs. The raw data were recorded on a high-bandwidth, high-memory-depth oscilloscope. Six continuous measurements were taken, separated by ~10-s data-saving periods. Colored circles at the start of each trace show the theoretical splitting of each third-sound mode pair for the best-fit initial vortex metastable distribution. Insets show spatial amplitude profiles of each third-sound mode.
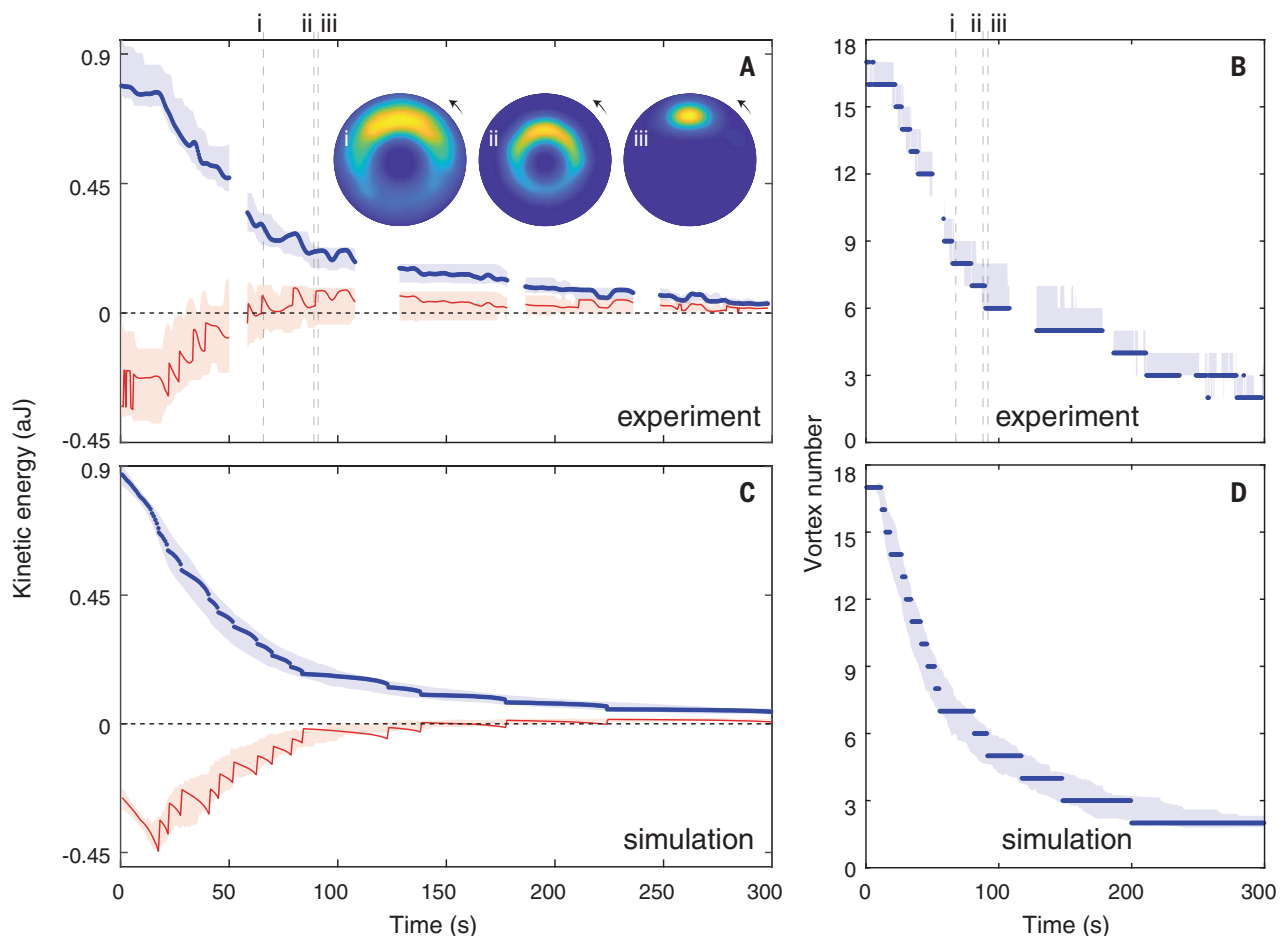
Fig. 4. Single-shot evolution of vortex-cluster metastable states. (**A**) Evolution of total kinetic energy (blue curve) and free-vortex cluster kinetic energy (red curve). Insets show metastable vortex probability densities at times indicated by the vertical dashed lines. These probability densities have the same color scale as those in Fig. 1C, with p_{max} = {0.0087, 0.015, 0.032} μm^{-2}, respectively, from left to right. The second and third metastable distributions are taken, respectively, just before and just after the 7-to-6 annihilation event. The angular momentum of each distribution is chosen, within the uncertainty window of the fit, to maximize the entropy of the state and therefore represents the most statistically likely of the experimentally plausible distributions. (**B**) Experimentally determined decay of the vortex number. Vertical dashed lines correspond to times in (A). Note that although these data display steps in the vortex number, this is a feature of our analysis that minimizes the root-mean-square uncertainty only over discrete vortex number. Our experiments approach single-vortex resolution; however, the continuous variation of vortex-induced splitting with time precludes direct unambiguous observation of individual steps in the splitting that result from creation or annihilation (*40*). (**C** and **D**) Point-vortex simulations of the system evolution [see section 3.3 of (*37*) for implementation]. (C) Evolution of the total (blue curve) and free-vortex (red curve) kinetic energies. (D) Evolution of the free-vortex number. In all traces, the shaded area corresponds to a 1-SD uncertainty.

energy essentially unchanged, as can be seen by the lack of discrete steps in the blue curves of Fig. 4, A and C. Therefore, annihilation events increase the kinetic energy of the free-vortex cluster by drawing energy out of the background flow. This pushes the cluster outward to a higher separation, as illustrated by the metastable states just before and after an annihilation event, as shown in insets ii and iii, respectively, in Fig. 4A.

In addition to allowing the observation of evaporative heating in a single continuous shot, our experiments allow the diffusivity D of vortices to be established in a regime for superfluid helium films, where it was previously inaccessible. The vortex diffusivity plays an important role in dynamic corrections to

the BKT transition (*10*) and in the dissipation of persistent flow (*47*). This has motivated substantial research efforts to quantify it both near the BKT transition and outside the regime of BKT superfluidity (*8, 34, 44*). However, achieving a high signal-to-noise ratio has generally proved challenging (*8*), and surface pinning is known to have a major influence on measurement outcomes (*34, 48*). By contrast, our experiments are not dominated by surface pinning [see section 6 of (*37*)] and achieve near-single-vortex resolution. From them, we obtain a value of $D = k_B T \alpha / \rho d\kappa \sim 100$ nm^2 s^{-1}, where k_B is the Boltzmann constant. This is five orders of magnitude below previous measurements for which the vortex dynamics are not dominated by pinning (*34*), verifying the

extrapolation from 30-year-old experimental observations that the diffusivity could become exceedingly small outside the BKT regime at low temperatures (*8*). Future experiments varying the temperature, film thickness, and surface properties may further elucidate the details of dissipation in thin superfluid helium films.

Concluding perspectives

The experiments reported here were enabled by the use of microscale confinement, which greatly enhances the interactions between vortices, between third-sound and vortices, and between third-sound and light. Interactions with strong pinning sites have previously prevented the observation of coherent vortex

dynamics in superfluid helium films (*42*). In our experiments, vortex-vortex interactions dominate because of the increased confinement and atomically smooth surface of the device. The smoothness of the surface results in a conservative upper bound to the vortex unpinning velocity of 0.2 cm/s [see section S6 of (*37*)], three orders of magnitude lower than previous experiments (*42*). As such, vortex-vortex interactions dominate even for the smallest possible clusters containing only two vortices. Furthermore, a four-order-of-magnitude enhancement in the interaction strength between vortices and third-sound compared with earlier experiments (*39*, *42*) allows resolution approaching the single-vortex level. Together, these capabilities provide a tool for future study of the rich dynamics of quasi–two-dimensional vortices in strongly interacting superfluids on a silicon chip. Vortex dynamics in the regime of BKT superfluidity may also be accessible by operating with thinner films.

The ability to nondestructively track vortex dynamics in a single shot opens the prospect to explore out-of-equilibrium dynamics and stochastic noise-driven processes that are challenging to study with other techniques (*16*, *49*). It also promises to resolve contentious aspects of vortex dynamics in strongly interacting superfluids, such as dissipation and diffusion models (*8*, *30*), vortex inertia (*27*, *28*), and the Iordanskii force (*29*). Furthermore, whereas the experiments reported here were performed with a relatively small number of vortices, the Angström scale of the vortex core in helium-4 will enable future research on the dynamics of ensembles of thousands of vortices, a regime well outside current capabilities with cold atom and exciton-polariton superfluids (*38*). This could allow emergent phenomena in two-dimensional turbulence, such as turbulent cascades (*38*) and anomalous hydrodynamics (*12*), to be explored.

REFERENCES AND NOTES

1. D. Mitra *et al.*, *Nat. Phys.* **14**, 173–177 (2017).
2. C. Gross, I. Bloch, *Science* **357**, 995–1001 (2017).
3. A. D. King *et al.*, *Nature* **560**, 456–460 (2018).
4. N. Chamel, *J. Astrophys. Astron.* **38**, 43 (2017).
5. STAR Collaboration, *Nature* **548**, 62–65 (2017).
6. P. W. Anderson, N. Itoh, *Nature* **256**, 25–27 (1975).
7. P. K. Kovtun, D. T. Son, A. O. Starinets, *Phys. Rev. Lett.* **94**, 111601 (2005).
8. P. W. Adams, W. I. Glaberson, *Phys. Rev. B* **35**, 4633–4652 (1987).
9. J. M. Kosterlitz, D. J. Thouless, *J. Phys. Chem.* **5**, L124–L126 (1972).
10. D. J. Bishop, J. D. Reppy, *Phys. Rev. Lett.* **40**, 1727–1730 (1978).
11. T. W. Neely *et al.*, *Phys. Rev. Lett.* **111**, 235301 (2013).
12. P. Wiegmann, A. G. Abanov, *Phys. Rev. Lett.* **113**, 034501 (2014).
13. D. V. Freilich, D. M. Bianchi, A. M. Kaufman, T. K. Langin, D. S. Hall, *Science* **329**, 1182–1185 (2010).
14. S. Donadello *et al.*, *Phys. Rev. Lett.* **113**, 065302 (2014).
15. A. Amo *et al.*, *Science* **332**, 1167–1170 (2011).
16. E. Estrecho *et al.*, *Nat. Commun.* **9**, 2944 (2018).
17. G. Gauthier *et al.*, *Science* **364**, 1264–1267 (2019).
18. S. P. Johnstone *et al.*, *Science* **364**, 1267–1271 (2019).
19. L. Onsager, *Nuovo Cim.* **6** (S2), 279–287 (1949).
20. P. Makotyn, C. E. Klauss, D. L. Goldberger, E. A. Cornell, D. S. Jin, *Nat. Phys.* **10**, 116–119 (2014).
21. M. W. Zwierlein, J. R. Abo-Shaeer, A. Schirotzek, C. H. Schunck, W. Ketterle, *Nature* **435**, 1047–1051 (2005).
22. C. Eigen *et al.*, *Nature* **563**, 221–224 (2018).
23. B. Ko, J. W. Park, Y. Shin, *Nat. Phys.* (2019).
24. E. Fonda, D. P. Meichle, N. T. Ouellette, S. Hormoz, D. P. Lathrop, *Proc. Natl. Acad. Sci. U.S.A.* **111** (Suppl 1), 4707–4710 (2014).
25. H. Hu, B. C. Mulkerin, U. Toniolo, L. He, X.-J. Liu, *Phys. Rev. Lett.* **122**, 070401 (2019).
26. F. Ancilotto *et al.*, *Int. Rev. Phys. Chem.* **36**, 621–707 (2017).
27. D. J. Thouless, J. R. Anglin, *Phys. Rev. Lett.* **99**, 105301 (2007).
28. T. Simula, *Phys. Rev. A* **97**, 023609 (2018).
29. E. B. Sonin, *Phys. Rev. B* **55**, 485–501 (1997).
30. L. Thompson, P. C. E. Stamp, *Phys. Rev. Lett.* **108**, 184501 (2012).
31. G. I. Harris *et al.*, *Nat. Phys.* **12**, 788–793 (2016).
32. A. Kashkanova *et al.*, *Nat. Phys.* **13**, 74–79 (2016).
33. A. Noury *et al.*, *Phys. Rev. Lett.* **122**, 165301 (2019).
34. K. A. Gillis, S. M. Volz, J. M. Mochel, *Phys. Rev. B* **40**, 6684–6694 (1989).
35. D. K. Armani, T. J. Kippenberg, S. M. Spillane, K. J. Vahala, *Nature* **421**, 925–928 (2003).
36. D. L. McAuslan *et al.*, *Phys. Rev. X* **6**, 021012 (2016).
37. Materials and methods are available as supplementary materials.
38. M. T. Reeves, T. P. Billam, X. Yu, A. S. Bradley, *Phys. Rev. Lett.* **119**, 184502 (2017).
39. F. M. Ellis, H. Luo, *Phys. Rev. B* **39**, 2703–2706 (1989).
40. S. Forstner *et al.*, *New J. Phys.* **21**, 053029 (2019).
41. C. G. Baker *et al.*, *New J. Phys.* **18**, 123025 (2016).
42. F. M. Ellis, L. Li, *Phys. Rev. Lett.* **71**, 1577–1580 (1993).
43. M. S. Hanay *et al.*, *Nat. Nanotechnol.* **10**, 339–344 (2015).
44. D. T. Ekholm, R. B. Hallock, *Phys. Rev. Lett.* **42**, 449–452 (1979).
45. A. I. Golov, P. M. Walmsley, *J. Low Temp. Phys.* **156**, 51–70 (2009).
46. E. Kozik, B. Svistunov, *Phys. Rev. Lett.* **100**, 195302 (2008).
47. L. Yu, *Phys. Rev.* **25**, 198–215 (1982).
48. G. Agnolet, D. F. McQueeney, J. D. Reppy, *Phys. Rev. B* **39**, 8934–8958 (1989).
49. S. Serafini *et al.*, *Phys. Rev. X* **7**, 021031 (2017).
50. Y. P. Sachkou *et al.*, Experimental and simulation datasets for: Coherent vortex dynamics in a strongly-interacting superfluid on a silicon chip, Version 1.0, Zenodo (2019); https://doi.org/10.5281/zenodo.3524827.
51. Y. P. Sachkou *et al.*, Data processing and simulation scripts for: Coherent vortex dynamics in a strongly-interacting superfluid on a silicon chip, Version 1.0, Zenodo (2019); https://doi.org/10.5281/zenodo.3524872.

Science

Coherent vortex dynamics in a strongly interacting superfluid on a silicon chip

Yauhen P. Sachkou, Christopher G. Baker, Glen I. Harris, Oliver R. Stockdale, Stefan Forstner, Matthew T. Reeves, Xin He,
David L. McAuslan, Ashton S. Bradley, Matthew J. Davis and Warwick P. Bowen

Following vortices around

When stirred, superfluids react by creating quantized vortices. Studying the dynamics of these vortices, especially
in the strongly interacting regime, is technically challenging. Sachkou *et al.* developed a technique for the nondestructive
tracking of vortices in thin films of superfluid helium-4. Their system contained a microtoroid optical cavity coated by a
thin film of helium-4, in which vortices were created by using laser light. When imaging the subsequent dynamics of the
vortices, the researchers found that coherent dynamics strongly dominated over dissipation.
        Science, this issue p. 1480

ARTICLE TOOLS	http://science.sciencemag.org/content/366/6472/1480
SUPPLEMENTARY MATERIALS	http://science.sciencemag.org/content/suppl/2019/12/18/366.6472.1480.DC1
REFERENCES	This article cites 76 articles, 7 of which you can access for free http://science.sciencemag.org/content/366/6472/1480#BIBL
PERMISSIONS	http://www.sciencemag.org/help/reprints-and-permissions

Use of this article is subject to the Terms of Service